Geophysical Research Letters

RESEARCH LETTER
10.1029/2022GL100143

Key Points:

- We calculate elastic tensors of olivine aggregates for four different slip systems and shear wave splitting parameters in the mantle wedge
- The hexagonal approximation of full elastic tensors is reasonable for most slip systems, particularly the A-type, and initial polarization
- The hexagonal approximation results in nearly identical tensors for A- and E-type and reduced delay time for C-type

Supporting Information:

Supporting Information may be found in the online version of this article.

Correspondence to:

L. M. Kenyon,
kenyo099@umn.edu

Citation:

Kenyon, L. M., & Wada, I. (2022). Shear-wave splitting in the mantle wedge: Role of elastic tensor symmetry of olivine aggregates. *Geophysical Research Letters*, *49*, e2022GL100143. https://doi.org/10.1029/2022GL100143

Received 21 JUN 2022
Accepted 4 OCT 2022

Shear-Wave Splitting in the Mantle Wedge: Role of Elastic Tensor Symmetry of Olivine Aggregates

L. M. Kenyon[1] and I. Wada[1]

[1]University of Minnesota Twin Cities, Minneapolis, MN, USA

Abstract Using a 3-D mantle wedge flow field for a generic oblique subduction system, we calculate elastic tensors of mineral aggregates in the mantle wedge for A-, B-, C-, and E-type olivine crystal preferred orientations (CPO) and apply the calculated elastic tensor in the forward calculation of shear-wave splitting (SWS) through the mantle wedge. We find that the hexagonal approximation of the full tensor does not affect the SWS parameters (the fast direction and the delay time) significantly for all CPO types except that the delay time for C-type CPO becomes shorter. Additionally, we find that despite the 3-D mantle flow field that results from oblique subduction, the fast direction is margin-normal for A-, C- and E-type CPOs and margin-parallel for B-type CPO.

Plain Language Summary As oceanic plates subduct, they drag the overlying mantle material, inducing mantle wedge flow. As the mantle flows, mineral crystals align in certain directions. Earthquake waves that pass through the aligned crystals travel faster in one direction than another. As a result, the waves split into two parts and are characterized by two parameters: fast direction and delay time. We can simplify how we model this material, but it may impact these parameters. In this study, we test the non-simplified and simplified material for four different directions of mineral alignment and calculate the fast direction and delay time for a 3-D mantle flow where the oceanic plate is moving toward the edge of another plate at an angle of 45°. We find that simplifying the material has modest effects on the parameters but simplification can cause smaller delay times for one mineral alignment direction, underestimating how aligned the minerals are. Overall, the mineral alignments result in fast directions that are mainly perpendicular to the edge of the overriding plate, which does not reflect the 3-D mantle wedge flow pattern.

1. Introduction

In the studies of shear wave splitting (SWS), the elastic tensor of mineral aggregates have commonly been approximated by hexagonally symmetric tensors (Browaeys & Chevrot, 2004). It is assumed that the hexagonal approximation is reasonable for aggregates of olivine and enstatite, which are the primary and common secondary minerals in the upper mantle, respectively, because the majority of the anisotropy comes from the hexagonal symmetry component of their elastic tensors (Bernard et al., 2021; Browaeys & Chevrot, 2004). Indeed, it has been shown that this hexagonal approximation is reasonable for estimating the fast polarization direction (hereafter referred to as the fast direction) and the delay time of SWS under ocean basins where the mantle flow direction is relatively uniform in the upper mantle (Becker et al., 2006). A similar approach has been applied to model SWS parameters in the mantle wedge of subduction zones (Confal et al., 2018; Faccenda & Capitanio, 2013; Levin et al., 2007). In some studies, full anisotropic elastic tensors are adopted in the SWS calculation (Kaminski & Okaya, 2018), and the difference between the applications of hexagonal approximation and full elastic tensors has not been quantified.

Several different types of olivine crystal preferred orientation (CPO) are observed both in natural samples and in lab experiments (Jung, 2017). With A- and E-type olivine CPOs that develop under simple shear, the *a*-axis of olivine crystals aligns sub-parallel to the long axis of the finite strain ellipsoid (FSE), but the orientations of the *b*- and *c*-axes differ between the two types (Skemer & Hansen, 2016). A-type CPO develops at relatively low stress and low water content, and E-type CPO develops at similarly low stress but higher water content (Jung & Karato, 2001; Karato et al., 2008). With B- and C-type CPOs, the olivine *c*-axis aligns sub-parallel to the FSE long axis, but the orientations of *a*- and *b*-axes differ between the two types. B-type CPO develops at high stress and moderate to high water content, and C-type CPO develops at low stress and high water content. With D-type CPO, the *a*-axis aligns sub-parallel to the FSE long axis, and it has multiple possible slip planes

that include those of A- and E-type CPOs (Jung & Karato, 2001; Karato et al., 2008). The multiple active slip planes result in a natural hexagonal symmetry where the *b*-axis and *c*-axis form girdles on pole plots, which is theoretically identical to the hexagonal approximation for both A- and E-type CPOs. For this reason, we exclude D-type in this study, which otherwise would be expected to form at high stress and low water content. In the mantle wedge, higher shear stresses and water contents may be present due to the corner flow and the dehydration of the subducting slab, and B-, C-, and E-type CPOs are most likely to form. However, CPO type is dependent on the strain history, rather than the amount of stress or water present at a given location, and the development of A-type CPO in the mantle wedge is possible (Bernard et al., 2019). Previous studies that performed forward SWS calculations for the mantle wedge indicate that A-, C- and E-type olivine CPOs result in margin-normal fast directions whereas B-type results in margin-parallel fast directions (Faccenda & Capitanio, 2013; Kaminski & Okaya, 2018). However, varying parameterization and assumptions in the calculations make it difficult to compare the impacts of different CPO types on SWS in the mantle wedge.

The choice of olivine CPO type and aggregates' elastic tensor symmetry can impact the forward SWS calculations. Using a velocity field that was calculated by Wada (2021) for three-dimensional (3-D) mantle wedge flow at oblique subduction zones, we calculate both the full elastic tensors and the tensors that consist of the hexagonal and isotropic components of the full tensors (hereafter referred to as the hexagonal tensors) in the mantle wedge for each of the A-, B-, C-, and E-type CPOs. We then perform forward calculation of the SWS parameters for the forearc, arc, and back-arc regions, using the calculated elastic tensors for the mantle wedge, and examine the variability in the SWS parameters with tensor symmetry and olivine CPO type.

2. Methods

Following Kenyon and Wada (2022a, 2022b), we first calculate the CPO in the mantle wedge for a given 3-D mantle wedge flow field, using a modified version of D-Rex (Kaminski et al., 2004). The obliquity of the incoming plate motion, which is measured relative to the margin-perpendicular direction in this study, has a primary control on the azimuthal directions of the mantle wedge inflow and outflow (Wada, 2021). In this study, we use the mantle flow model from Wada (2021) for a subduction zone with an obliquity of 45° and a true slab dip of 45° (apparent slab dip of 35° parallel to the subduction direction). The D-Rex calculation is performed for an aggregate of 1,000 crystals that are 70% olivine and 30% enstatite. We begin the calculation with crystals in random orientation and track the strain that accumulates along flow streamlines until either the strain reaches 10 or the elapsed time reaches 5 million years. The latter time constraint prevents unreasonable accumulation of strain in the nearly stagnant mantle immediately below the crust. We calculate the full anisotropic elasticity tensors on a 10-km by 10-km grid on a vertical plane parallel to the subduction direction. Increasing pressure and temperature have competing effects on elastic moduli (Abramson et al., 1997; Anderson & Isaak, 1995), and their effects are likely to be small along an adiabatic temperature gradient (Abt & Fischer, 2008; Faccenda & Capitanio, 2013; Mainprice, 2007). We use elastic moduli that are reported by Abramson et al. (1997) and Weidner et al. (1978) for olivine and enstatite, respectively, for all depths (Table S1 in Supporting Information S1). A CPO type is chosen as input to the calculation for D-Rex by assigning reference dimensionless resolved shear stresses (RSS) (Table S2 in Supporting Information S1). Multiple slip systems have been reported for enstatite (Bernard et al., 2021; Jung et al., 2010). If more than 40% of the aggregate is olivine, the effect of enstatite on the orientation of aggregates' anisotropy is relatively small while it may impact the strength of anisotropy (Bernard et al., 2021). For simplicity, we choose to use one CPO for enstatite for all calculations and neglect the variation in the strength of anisotropy due to the choice of enstatite CPO. Other D-Rex free parameters are listed in Table S3 in Supporting Information S1.

We construct vertical columns that extend from the slab surface to the Moho. Each column consists of 10-km-thick uniformly anisotropic horizontal layers that are assumed to be infinitely wide for the calculation purpose, and each layer is assigned a calculated full elastic tensor (Kenyon & Wada, 2022a, 2022b). We calculate the SWS parameters, assuming vertical S wave propagation through the vertical columns. We perform the same SWS calculations using the hexagonal tensors, which are calculated from the full tensors by using the principles of decomposition of the elastic tensor (Browaeys & Chevrot, 2004) and the Gaussian wavelet method implemented in the MSAT toolbox (Walker & Wookey, 2012). The SWS parameters are calculated at a frequency of 0.5 Hz to simulate local S waves (Long & Wirth, 2013). The SWS calculation is based on the eigenvalue minimization method of Silver and Chan (1991). The SWS parameters vary with the initial polarization of the shear waves and

the incidence angle of the ray path (Silver & Savage, 1994). We calculate the SWS parameters over a full range of initial polarization but for a vertical ray path (0° incidence angles) to reduce the number of model parameters. However, the impact of the incidence angle on the SWS parameters is relatively small if the angle is 10° (Kenyon & Wada, 2022a). In some layers, particularly in the shallowest portion of the domain, the speeds of the fast and slow components of S waves (Vs_{fast} and Vs_{slow}, respectively) are nearly identical and thus isotropic. In our SWS calculations, any layers with $Vs_{slow}/Vs_{fast} > 0.99$ are removed for computational efficiency.

In this paper, SWS calculations are performed for the forearc, arc, and back-arc regions, which we defined to be where the slab surface depth is 80–90, 100–110, and 120 km, respectively. The slab surface depth does not correspond to the thickness of the anisotropic material that overlies the subducting slab in our calculation as we exclude the overriding crust and the layers that are nearly isotropic.

3. Results

To present the calculated CPO, we use the axis of symmetry of the hexagonal component of the full tensor, which is referred to as the transverse isotropic (TI) axis (Figure 1). The TI axis approximately corresponds to the fast axis of the full tensor and thus the average fast axis of the mineral aggregates unless the tensor is nearly isotropic (Figure 2). For hexagonal tensors, the TI axis is the fast axis.

The distributions of A- and E-type CPOs in the mantle wedge are similar, and in map view, their TI axes do not align with the mantle flow azimuth in many parts of the mantle wedge and are highly spatially variable (Figure 1). This is attributed to the 3-D mantle wedge flow pattern due to oblique subduction, making the common assumption of their alignment with the flow direction invalid as previously reported (Faccenda & Capitanio, 2013; Jadamec & Billen, 2010; Kenyon & Wada, 2022a). The TI axis of B-type CPO is largely perpendicular to the flow direction and horizontal whereas that of C-type CPO is also perpendicular to the flow direction but is nearly vertical, consistent with the results of previous studies (Skemer & Hansen, 2016).

To examine the impact of the hexagonal approximation for each CPO type, we calculate the strength of anisotropy for both the full and hexagonal tensors at a location in the mantle wedge where the strain history is largely of horizontal shear and relatively simple to make the comparison between CPO types and tensor symmetries easier (Figure 2). The hexagonal approximation results in a modest change to the overall distribution of the strength of anisotropy for A- and E-type CPOs but a more significant change for B- and C-type CPOs. In particular, the strength of anisotropy is noticeably reduced for some wave propagation directions for B- and C-type CPOs relative to the full tensor, potentially leading to underestimation of the delay time.

The SWS calculations indicate that for both full and hexagonal tensors of A- and E-type CPOs, the fast direction is generally margin-perpendicular (Figures 3a and 4). However, when the initial polarization direction is approximately 25°–50°, sub-parallel to the margin, the fast direction in the forearc and the arc region shifts toward the margin-parallel direction. The delay time can vary with the initial polarization by a factor of 3–10 at a given location, but it generally increases from the forearc to the back-arc (Figure 3b). For A-type CPO, the SWS parameters for the hexagonal tensors are identical to those for the full tensor across the system and over the full range of initial polarizations, indicating that the hexagonal approximation is reasonable (Figures 3a and 3b). For E-type CPO, the SWS parameters for the hexagonal and full tensors are also similar, but those for the hexagonal tensors are more similar to those for A-type CPO (either full or hexagonal) tensors than to those for E-type CPO full tensors (Figures 3a and 3b). This indicates that under the hexagonal approximation, A- and E-type CPOs are largely indistinguishable. The larger difference between the full and the hexagonal tensors for E-type CPO likely indicates that there is a larger contribution from non-hexagonal symmetry components to the full tensor than for A-type CPO, for example, due to the presence of enstatite. A large difference between the hexagonal and full tensors for E-type CPO can result over a narrow range of initial polarization (e.g., ~80° difference for 38° initial polarization in the arc region). The eigenvalue minimization method that is employed in this study is known to result in overestimation of delay times and inadvertent time shifting of the wavelets by a half-wavelength, whose consequence is referred to as "cycle skipping" (Rümpker & Silver, 1998; Walsh et al., 2013). These may exaggerate the magnitude of the differences in the fast direction and the delay time between the hexagonal and full tensors at a given initial polarization (Kenyon & Wada, 2022a).

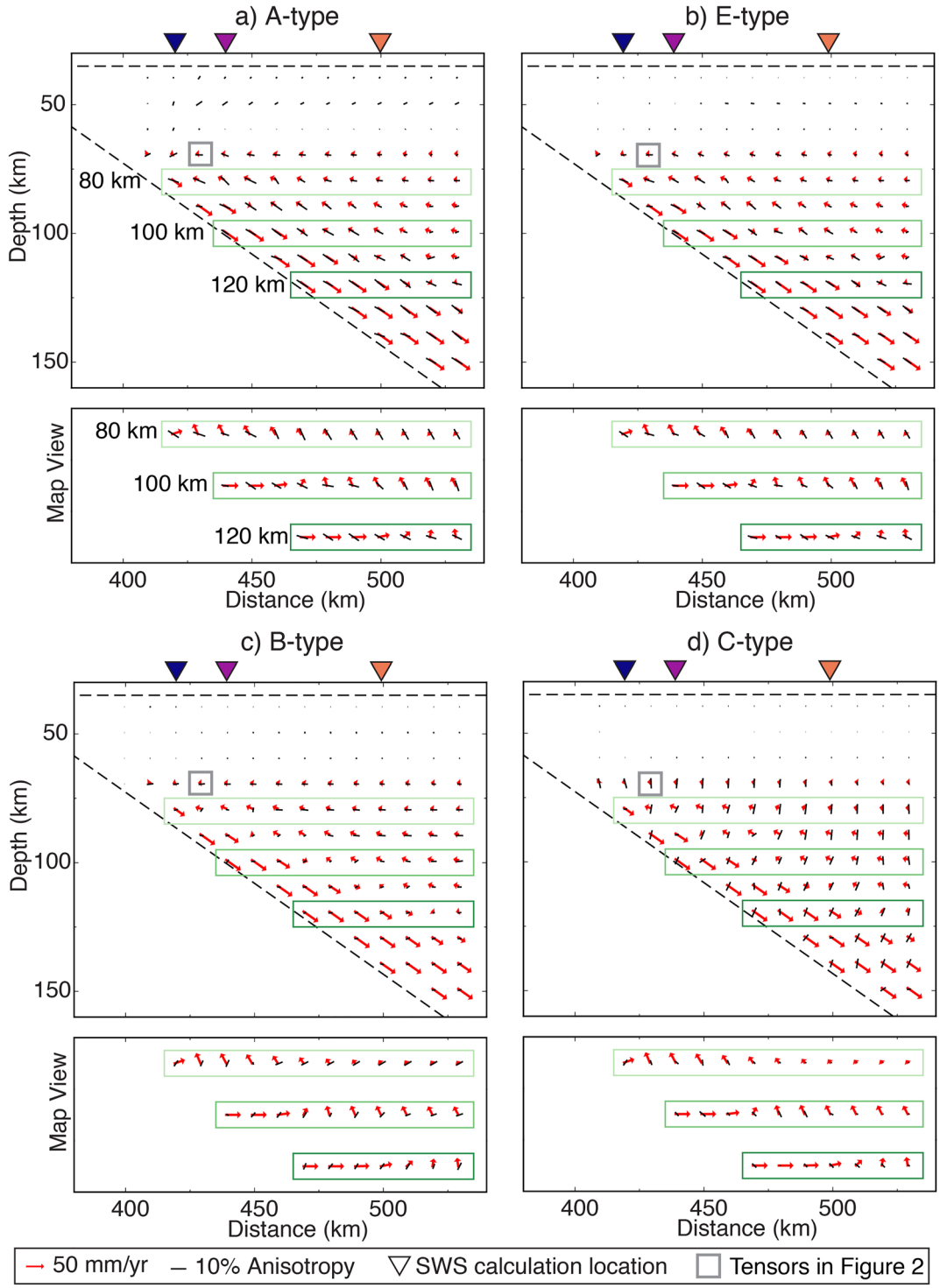

Figure 1. Velocity vector (red arrows) and average transverse isotropic axis (black bars) projected onto a vertical plane (top panel) and horizontal planes (bottom panel) at 80-, 100-, and 120-km depths for (a) A-type, (b) E-type, (c) B-type and (d) C-type olivine crystal preferred orientations. Gray square indicates the location used for the sample calculations of anisotropy strength (Figure 2). Blue, purple, and orange inverted triangles at the top indicate the columns for which shear-wave splitting calculations are performed for the forearc, arc, and back-arc regions, respectively (Figure 3).

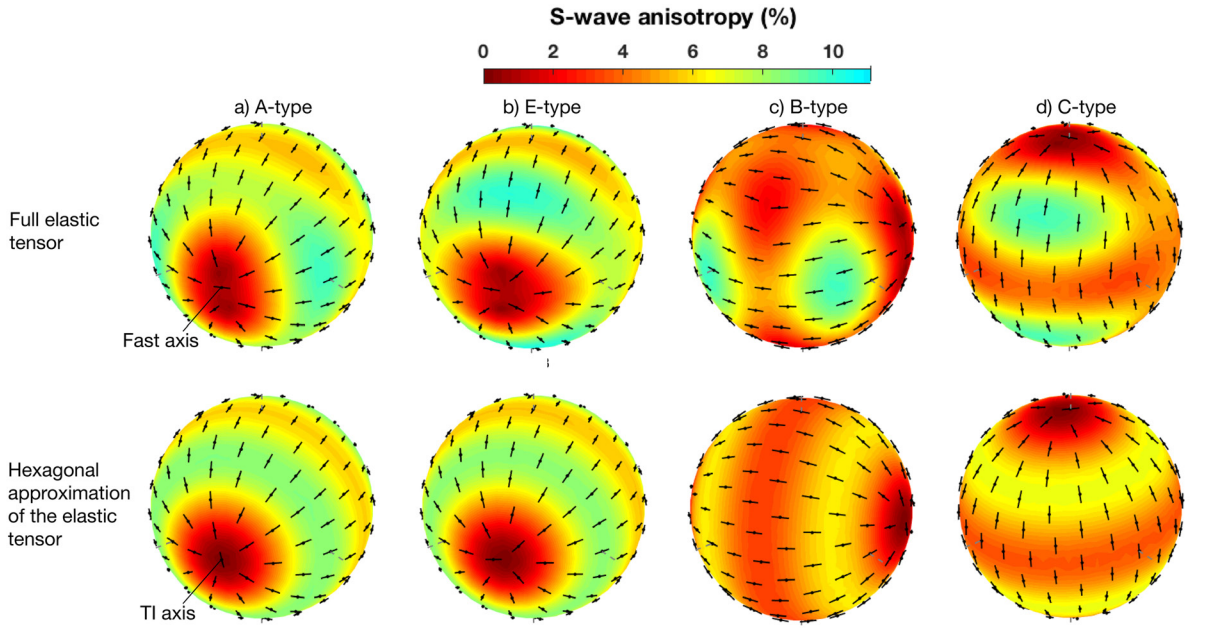

Figure 2. S-wave anisotropy (%) based on (top) the full elastic tensor and (bottom) the hexagonal tensor of olivine-enstatite aggregates with (a) A-type, (b) E-type, (c) B-type, and (d) C-type olivine crystal preferred orientations at a location shown in Figure 1.

The full and hexagonal tensors of B-type CPO result in similar SWS parameter values regardless of the location. The fast direction is generally margin-parallel except when the initial polarization direction is approximately 25°–50°, sub-parallel to the margin (Figures 3c and 4). Compared to A- and E-type CPOs, there is less variation in the fast direction with location for B-type CPO. The delay time varies with initial polarization but generally increases from the forearc to back-arc as in A- and E-type CPOs. However, the delay time is for the most part shorter than A- or E-type CPO at a given location (Figure 3d), which is consistent with the expectation that B-type CPO is generally less anisotropic (Figure 2).

For both full and hexagonal tensors of C-type CPOs, the fast direction is generally margin-normal except when the initial polarization direction is approximately 25–50°, sub-parallel to the margin (Figures 3c and 4). Overall, there is less variation in the fast direction in the back-arc than in the forearc, but back-arc delay times are generally larger than in the forearc and arc regions (Figure 3f). Compared to A- and E-type CPOs, the delay times for C-type CPO is smaller (Figure 3). This is expected given the nearly vertical fast axis, which results in a smaller difference between Vs_{fast} and Vs_{slow}. In our study, in particular, layers with small difference between Vs_{fast} and Vs_{slow} are excluded from the SWS calculations, potentially making the delay time even smaller in some locations. The C-type hexagonal tensors result in even smaller delay times than full tensor C-type CPO at all locations.

4. Discussion

Our results indicate that the differences in SWS parameters between full and hexagonal tensors are relatively small, and the hexagonal approximation is reasonable for most CPO types and initial polarization. However, over a relatively narrow range of initial polarization, the SWS parameters for B-, C-, and E-type CPOs can be noticeably different from those for the full tensor, and therefore the knowledge of initial polarization can be important when comparing the observed SWS parameters to predicted SWS parameters based on hexagonal approximation. Further, our study indicates that the hexagonal approximation impacts the delay time more than the fast directions. This is consistent with a previous SWS tomography study that examines the effects of hexagonal and orthorhombic symmetries on SWS splitting (Abt & Fischer, 2008). They found that assuming a hexagonal symmetry for the elastic tensor instead of orthorhombic symmetry leads to nearly identical fast directions, but up to 25% difference in the delay time.

In the forward modeling of SWS in subduction zones, there are some instances where the hexagonal approximation to the full tensors should be avoided. First, the hexagonal approximation of a single crystal olivine elastic

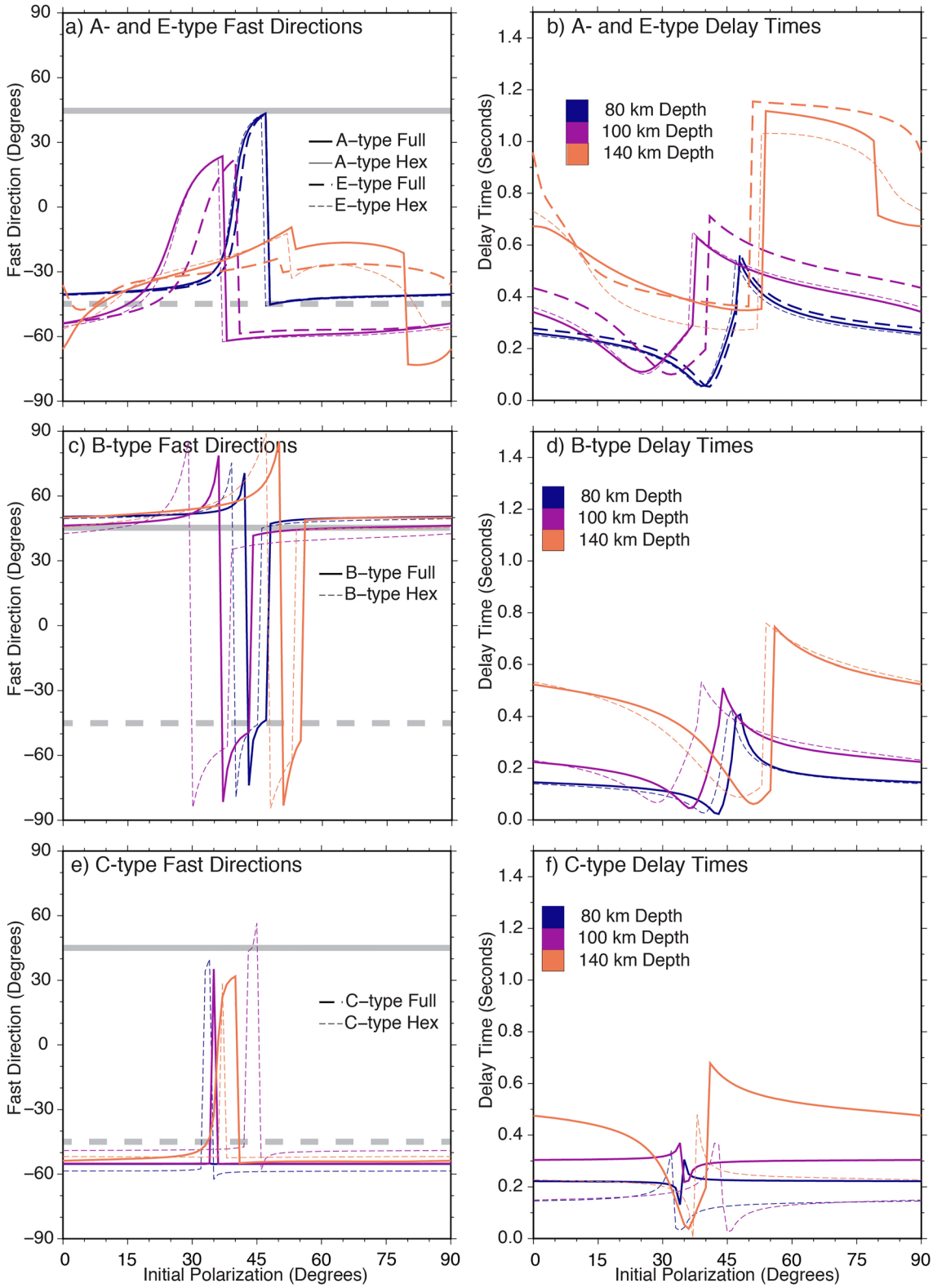

Figure 3. (a, c, e) Fast directions and (b, d, f) delay times over a full range of initial polarizations with a vertical incidence for (a)–(b) A- and E-type, (c)–(d) B-type, and (e)–(f) C-type olivine CPOs. Thick and thin lines indicate the full and hexagonal tensors, respectively. Color indicates the approximate depth to the slab surface and corresponds to the color of the inverted triangles in Figure 2. Lines for A-type full tensors and hexagonal tensors are nearly identical and overlap in both (a) and (b). Solid and dashed gray lines in (a, c, e) indicate margin-parallel and margin-normal directions, respectively.

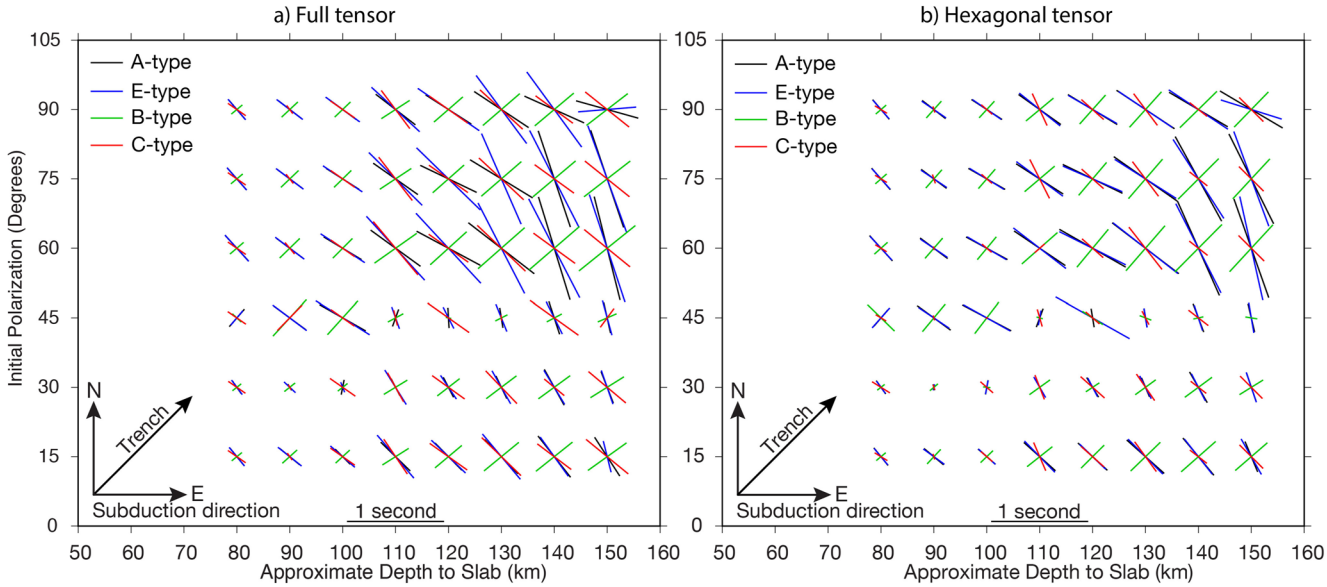

Figure 4. Calculated fast directions and delay times for (a) the full tensors and (b) the hexagonal tensors in map view for different locations and initial polarizations. Black, blue, green, and red bars indicate A-, E-, B-, and C-type olivine CPOs, respectively.

tensor results in an identical tensor for A- and E-type CPOs as the olivine *b*- and *c*-axes are averaged together. The hexagonal approximation to the aggregates' tensors are not identical for A- and E-type CPOs because of the difference in their slip systems and the presence of an anisotropic secondary phase, but they are very similar (Figure 2). Therefore, one should not use the hexagonal approximation for assessing the contributions of A- and E-type CPOs on SWS as they become indifferentiable. Second, for olivine aggregates with weak or undeveloped CPO, a hexagonal symmetry with the TI axis representing the fast axis is not a good approximation because the full tensor may be nearly isotropic and the fast axis may not be appropriately represented by the TI axis of its hexagonal component (Faccenda & Capitanio, 2013). In our model, weakly strained, nearly isotropic mantle material in the top few layers are excluded from the SWS calculations.

Previous local SWS studies indicate that the fast direction in the Alaska and Sumatra subduction zones is margin-normal in the arc and back-arc and margin-parallel in the forearc and that the delay times range from ~0.05 to 0.8 s with a weak positive correlation with the travel distance through the mantle wedge (Collings et al., 2013; Richards et al., 2021). Our study also indicates an overall increase in delay times with the depth to the slab surface regardless of the variation in the fast direction with depth as the delay time accumulates along the ray path unless the fast axis of a given layer coincides with the slow axis of another (i.e., the fast axis orientation is offset by ~90°), canceling out each other's anisotropy. The local SWS studies assume A-type olivine and attribute the margin-normal fast direction to 2-D margin-normal mantle wedge flow despite oblique subduction that likely results in 3-D mantle wedge flow. Our results show that in 3-D mantle wedge flow at oblique subduction zones, A-, C- and E-type CPOs all result in mainly margin-normal fast directions for both full and hexagonal tensors. B-type CPO could explain the margin-parallel fast directions in the forearc.

Anisotropy sources other than olivine likely contribute to observed SWS parameters. For example, some minerals in the crust, the cold nose of the mantle wedge, and along the subduction interface, such as amphibolite, chlorite, antigorite, phengite and talc, are strongly anisotropic and may contribute to margin-parallel fast directions (Ha et al., 2019; Jung, 2017; Katayama et al., 2009; Lee et al., 2020; Uchida et al., 2020). Many of the predicted delay times in this study are relatively small, particularly in the forearc. Small delay times in observed SWS data would be difficult to interpret in terms of mantle wedge anisotropy, given the noise and other potential sources of anisotropy. The predicted differences in delay times due to CPO types (and tensor symmetries) are even smaller, making it difficult to differentiate their variations in observed data based on delay times.

Our results indicate that any one of the four CPO types cannot explain the observed variation in SWS parameters between subduction zones and from the forearc to the back-arc within a subduction zone. The olivine CPO type

within the mantle wedge is likely to vary spatially as stress, water content, temperature, and strain geometry can vary over relatively short distances (Bernard et al., 2019; Karato et al., 2008). A 2-D study that incorporates spatial variation of olivine CPO type in the mantle wedge predicts spatial changes in the SWS fast direction that are similar to those observed in the Lau back-arc basin in the Tonga subduction zone (Kaminski & Okaya, 2018). In our model, the effect of spatial variation of CPO type is not included. Multiple CPO types can be incorporated to explain observations, but their variation should be consistent with the stress, water content, temperature, and strain geometry based the experimental data. In such a study, the hexagonal approximation can exaggerate the similarity or differences between different CPO types and may potentially contribute to the overall uncertainties.

In anisotropic P-wave seismic tomography, hexagonal tenors are used for 3-D ray tracing in the inversion with a priori anisotropy (Bezada et al., 2016; Confal et al., 2020; Lee et al., 2021), and in the inversion for the anisotropic field, hexagonal tensors must be assumed to reduce the number of free parameters (Huang et al., 2015; Wang & Zhao, 2013). Some recent studies solve for the 3-D orientation of a hexagonal tensor but assume the TI axis to be the slow axis and a fast plane orthogonal to the TI axis (Wang & Zhao, 2021; Wang et al., 2022). This assumption is reasonable for anisotropy caused by parallel faults and melt lenses. For anisotropy caused by olivine CPO, the TI axis corresponds more closely to the fast axis of olivine aggregates (Figure 2). Future studies that solve for the fast axis will allow direct comparisons of the results to those based on forward modeling of olivine CPO in the mantle wedge.

5. Conclusions

For a given 3-D mantle wedge flow field, we calculate the elastic tensors of mineral aggregates for four different olivine CPO types and SWS parameters using the full and simplified hexagonal tensors. The calculated CPO distributions indicate that the fast axis of the mineral aggregates in the inflow region of the mantle wedge is generally sub-parallel to the flow direction for A- and E-type CPOs and perpendicular to the flow direction for B- and C-type CPOs. However, in other parts of the mantle wedge, the orientation of the fast axis relative to the flow direction is more variable. In the SWS calculation, the hexagonal approximation is generally reasonable for the fast directions of all CPO types, but the impact of the approximation is larger for B-, C-, and E-type CPOs compared to that for A-type. In particular, hexagonal approximation for C-type CPO can reduce delay times, leading to underestimation of anisotropy strength. The hexagonal approximation of E-type CPO results in nearly identical SWS results to those of A-type CPO. The margin-normal fast direction that is observed in some subduction zones with oblique convergence could be explained by either of A-, E- or C-type CPO whereas the margin-parallel fast direction could be explained by B-type CPO.

Data Availability Statement

The codes that were used in this study are the modified versions of D-Rex (Kaminski et al., 2004) and MATLAB Seismic Anisotropy Toolkit (Walker & Wookey, 2012), both of which are available on Zenodo (https://doi.org/10.5281/zenodo.7153285; Kenyon & Wada, 2022b). Some figures were generated using Generic Mapping Tool (Wessel et al., 2013) and MSAT. The tables that summarize the elastic moduli for olivine and enstatite and the reference dimensionless RSS for different olivine CPO types and enstatite are found in Supporting Information S1.

Acknowledgments
We thank Maximiliano Bezada, Lars Hansen, and Zhao Zhu for discussions during the early phase of this research. We also thank Haemyeong Jung and Vadim Levin for thorough review, which improved the manuscript. This research was partially funded by NSF EAR-1620604 to I.W.

References

Abramson, E. H., Brown, J. M., Slutsky, L. J., & Zaug, J. (1997). The elastic constants of San Carlos olivine to 17 GPa. *Journal of Geophysical Research*, *102*(B6), 12253–12263. https://doi.org/10.1029/97JB00682

Abt, D. L., & Fischer, K. M. (2008). Resolving three-dimensional anisotropic structure with shear wave splitting tomography. *Geophysical Journal International*, *173*(3), 859–886. https://doi.org/10.1111/j.1365-246X.2008.03757.x

Anderson, O. L., & Isaak, D. G. (1995). Elastic constants of mantle minerals at high temperature (pp. 64–97). https://doi.org/10.1029/RF002p0064

Becker, T. W., Chevrot, S., Schulte-Pelkum, V., & Blackman, D. K. (2006). Statistical properties of seismic anisotropy predicted by upper mantle geodynamic models. *Journal of Geophysical Research*, *111*(8), 1–16. https://doi.org/10.1029/2005JB004095

Bernard, R. E., Behr, W. M., Becker, T. W., & Young, D. J. (2019). Relationships between Olivine CPO and deformation parameters in naturally deformed rocks and implications for Mantle seismic anisotropy. *Geochemistry, Geophysics, Geosystems*, *20*(7), 3469–3494. https://doi.org/10.1029/2019GC008289

Bernard, R. E., Schulte-pelkum, V., & Behr, W. M. (2021). Tectonophysics the competing effects of olivine and orthopyroxene CPO on seismic anisotropy. *Tectonophysics*, *814*, 228954. https://doi.org/10.1016/j.tecto.2021.228954

Bezada, M. J., Faccenda, M., & Toomey, D. R. (2016). Representing anisotropic subduction zones with isotropic velocity models: A characterization of the problem and some steps on a possible path forward. *Geochemistry, Geophysics, Geosystems*, *17*(8), 3164–3189. https://doi.org/10.1002/2016GC006507

Browaeys, J. T., & Chevrot, S. (2004). Decomposition of the elastic tensor and geophysical applications. *Geophysical Journal International*, *159*(2), 667–678. https://doi.org/10.1111/j.1365-246X.2004.02415.x

Collings, R., Rietbrock, A., Lange, D., Tilmann, F., Nippress, S., & Natawidjaja, D. (2013). Seismic anisotropy in the Sumatra subduction zone. *Journal of Geophysical Research: Solid Earth*, *118*(10), 5372–5390. https://doi.org/10.1002/jgrb.50157

Confal, J. M., Bezada, M. J., Eken, T., Faccenda, M., Saygin, E., & Taymaz, T. (2020). Influence of upper Mantle anisotropy on isotropic P-wave tomography images obtained in the eastern mediterranean region. *Journal of Geophysical Research: Solid Earth*, *125*(8), 1–21. https://doi.org/10.1029/2019JB018559

Confal, J. M., Faccenda, M., Eken, T., & Taymaz, T. (2018). Numerical simulation of 3-D mantle flow evolution in subduction zone environments in relation to seismic anisotropy beneath the eastern Mediterranean region. *Earth and Planetary Science Letters*, *497*, 50–61. https://doi.org/10.1016/j.epsl.2018.06.005

Faccenda, M., & Capitanio, F. A. (2013). Seismic anisotropy around subduction zones: Insights from three-dimensional modeling of upper mantle deformation and SKS splitting calculations. *Geochemistry, Geophysics, Geosystems*, *14*(1), 243–262. https://doi.org/10.1002/ggge.20055

Ha, Y., Jung, H., & Raymond, L. A. (2019). Deformation fabrics of glaucophane schists and implications for seismic anisotropy: The importance of lattice preferred orientation of phengite. *International Geology Review*, *61*(6), 720–737. https://doi.org/10.1080/00206814.2018.1449142

Huang, Z., Zhao, D., & Wang, L. (2015). P wave tomography and anisotropy beneath Southeast Asia: Insight into mantle dynamics. *Journal of Geophysical Research: Solid Earth*, *120*(7), 5154–5174. https://doi.org/10.1002/2015JB012098

Jadamec, M. A., & Billen, M. I. (2010). Reconciling surface plate motions with rapid three-dimensional mantle flow around a slab edge. *Nature*, *465*(7296), 338–341. https://doi.org/10.1038/nature09053

Jung, H. (2017). Crystal preferred orientations of olivine, orthopyroxene, serpentine, chlorite, and amphibole, and implications for seismic anisotropy in subduction zones: A review. *Geosciences Journal*, *21*(6), 985–1011. https://doi.org/10.1007/s12303-017-0045-1

Jung, H., & Karato, S. (2001). Water-induced fabric transitions in olivine. *Science*, *293*(5534), 1460–1463. https://doi.org/10.1126/science.1062235

Jung, H., Park, M., Jung, S., & Lee, J. (2010). Lattice preferred orientation, water content, and seismic anisotropy of orthopyroxene. *Journal of Earth Sciences*, *21*(5), 555–568. https://doi.org/10.1007/s12583-010-0118-9

Kaminski, E., & Okaya, D. A. (2018). How to detect water in the Mantle wedge of a subduction zone using seismic anisotropy. *Geophysical Research Letters*, *45*(24), 13298–13305. https://doi.org/10.1029/2018GL079571

Kaminski, E., Ribe, N. M., & Browaeys, J. T. (2004). D-Rex, a program for calculation of seismic anisotropy due to crystal lattice preferred orientation in the convective upper mantle. *Geophysical Journal International*, *158*(2), 744–752. https://doi.org/10.1111/j.1365-246X.2004.02308.x

Karato, S., Jung, H., Katayama, I., & Skemer, P. (2008). Geodynamic significance of seismic anisotropy of the upper Mantle: New insights from laboratory studies. *Annual Review of Earth and Planetary Sciences*, *36*(1), 59–95. https://doi.org/10.1146/annurev.earth.36.031207.124120

Katayama, I., Hirauchi, K. I., Michibayashi, K., & Ando, J. I. (2009). Trench-parallel anisotropy produced by serpentine deformation in the hydrated mantle wedge. *Nature*, *461*(7267), 1114–1117. https://doi.org/10.1038/nature08513

Kenyon, L. M., & Wada, I. (2022a). Mantle wedge seismic anisotropy and shear wave splitting: Effects of oblique subduction. *Journal of Geophysical Research: Solid Earth*, *127*(4), 1–18. https://doi.org/10.1029/2021jb022752

Kenyon, L. M., & Wada, I. (2022b). Package for calculating crystal preferred orientation and local shear wave splitting for 3-D mantle wedge flow in subduction zones. *Zenodo*. https://doi.org/10.5281/zenodo.7153285

Lee, H., Bezada, M. J., & Faccenda, M. (2021). Can sub-slab low-velocity anomalies be an artifact caused by anisotropy? A case study from the Alboran slab area in the western mediterranean. *Tectonophysics*, *819*(January), 229080. https://doi.org/10.1016/j.tecto.2021.229080

Lee, J., Jung, H., Klemd, R., Tarling, M. S., & Konopelko, D. (2020). Lattice preferred orientation of talc and implications for seismic anisotropy in subduction zones. *Earth and Planetary Science Letters*, *537*, 116178. https://doi.org/10.1016/j.epsl.2020.116178

Levin, V., Okaya, D., & Park, J. (2007). Shear wave birefringence in wedge-shaped anisotropic regions. *Geophysical Journal International*, *168*(1), 275–286. https://doi.org/10.1111/j.1365-246X.2006.03224.x

Long, M. D., & Wirth, E. A. (2013). Mantle flow in subduction systems: The mantle wedge flow field and implications for wedge processes. *Journal of Geophysical Research: Solid Earth*, *118*(2), 583–606. https://doi.org/10.1002/jgrb.50063

Mainprice, D. (2007). Seismic anisotropy of the deep Earth from a mineral and rock physics perspective. *Treatise on Geophysics*, *2*, 437–491. https://doi.org/10.1016/B978-044452748-6.00045-6

Richards, C., Tape, C., Abers, G. A., & Ross, Z. E. (2021). Anisotropy variations in the Alaska subduction zone based on shear-wave splitting from intraslab earthquakes. *Geochemistry, Geophysics, Geosystems*, *22*(5), 1–18. https://doi.org/10.1029/2020GC009558

Rümpker, G., & Silver, P. G. (1998). Apparent shear-wave splitting parameters in the presence of vertically varying anisotropy. *Geophysical Journal International*, *135*(3), 790–800. https://doi.org/10.1046/j.1365-246X.1998.00660.x

Silver, P. G., & Chan, W. W. (1991). Shear wave splitting and subcontinental mantle deformation. *Journal of Geophysical Research*, *96*(B10), 16429. https://doi.org/10.1029/91JB00899

Silver, P. G., & Savage, M. K. (1994). The interpretation of shear-wave splitting parameters in the presence of two anisotropic layers. *Geophysical Journal International*, *119*(3), 949–963. https://doi.org/10.1111/j.1365-246X.1994.tb04027.x

Skemer, P., & Hansen, L. N. (2016). Inferring upper-mantle flow from seismic anisotropy: An experimental perspective. *Tectonophysics*, *668–669*, 1–14. https://doi.org/10.1016/j.tecto.2015.12.003

Uchida, N., Nakajima, J., Wang, K., Takagi, R., Yoshida, K., Nakayama, T., et al. (2020). Stagnant forearc mantle wedge inferred from mapping of shear-wave anisotropy using S-net seafloor seismometers. *Nature Communications*, *11*(1), 5676. https://doi.org/10.1038/s41467-020-19541-y

Wada, I. (2021). A simple picture of mantle wedge flow patterns and temperature variation. *Journal of Geodynamics*, *146*, 101848. https://doi.org/10.1016/j.jog.2021.101848

Walker, A. M., & Wookey, J. (2012). MSAT—A new toolkit for the analysis of elastic and seismic anisotropy. *Computers & Geosciences*, *49*, 81–90. https://doi.org/10.1016/j.cageo.2012.05.031

Walsh, E., Arnold, R., & Savage, M. K. (2013). Silver and Chan revisited. *Journal of Geophysical Research: Solid Earth*, *118*(10), 5500–5515. https://doi.org/10.1002/jgrb.50386

Wang, J., & Zhao, D. (2013). P-wave tomography for 3-D radial and azimuthal anisotropy of Tohoku and Kyushu subduction zones. *Geophysical Journal International*, *193*(3), 1166–1181. https://doi.org/10.1093/gji/ggt086

Wang, Z., & Zhao, D. (2021). 3D anisotropic structure of the Japan subduction zone. *Science Advances*, *7*, eabc9620. https://doi.org/10.1126/sciadv.abc9620

Wang, Z., Zhao, D., & Chen, X. (2022). Seismic anisotropy and intraslab hydrated faults beneath the NE Japan forearc. *Geophysical Research Letters*, *49*(2), 1–10. https://doi.org/10.1029/2021GL097266

Weidner, D. J., Wang, H., & Ito, J. (1978). Elasticity of orthoenstatite. *Physics of the Earth and Planetary Interiors*, *17*(2), P7–P13. https://doi.org/10.1016/0031-9201(78)90043-2

Wessel, P., Smith, W. H. F., Scharroo, R., Luis, J., & Wobbe, F. (2013). Generic mapping tools: Improved version released. *EOS, Transactions American Geophysical Union*, *94*(45), 409–410. https://doi.org/10.1002/2013EO450001